

## RESEARCH LETTER

10.1002/2017GL073687

## Key Points:

- Independent Component Analysis of GPS time series detects small tectonic deformation transient in slow strain-rates region
- Seismic and geodetic data reveal large aseismic contribution for a swarm-like activity in a normal fault environment
- The transient slip decreased Coulomb stress on the locked portion of an active low-angle normal fault

## Supporting Information:

- Supporting Information S1

## Correspondence to:

A. Gualandi,  
gualandi@caltech.edu

## Citation:

Gualandi, A., C. Nichele, E. Serpelloni, L. Chiaraluca, L. Anderlini, D. Latorre, M. E. Belardinelli, and J.-P. Avouac (2017), Aseismic deformation associated with an earthquake swarm in the northern Apennines (Italy), *Geophys. Res. Lett.*, *44*, doi:10.1002/2017GL073687.

Received 31 MAR 2017

Accepted 11 JUL 2017

Accepted article online 17 JUL 2017

## Aseismic deformation associated with an earthquake swarm in the northern Apennines (Italy)

A. Gualandi<sup>1</sup> , C. Nichele<sup>2</sup>, E. Serpelloni<sup>3</sup> , L. Chiaraluca<sup>3</sup> , L. Anderlini<sup>3</sup> , D. Latorre<sup>3</sup> , M. E. Belardinelli<sup>2</sup> , and J.-P. Avouac<sup>1</sup> 

<sup>1</sup>Department of Geology and Planetary Sciences, California Institute of Technology, Pasadena, California, USA, <sup>2</sup>University of Bologna, Dipartimento di Fisica e Astronomia, Settore di Geofisica, Italy, <sup>3</sup>Istituto Nazionale di Geofisica e Vulcanologia, Rome, Italy

**Abstract** Analyzing the displacement time series from continuous GPS (cGPS) with an Independent Component Analysis, we detect a transient deformation signal that correlates both in space and time with a seismic swarm activity (maximum  $M_w = 3.69 \pm 0.09$ ) occurred in the hanging wall of the Altotiberina normal fault (Northern Apennines, Italy) in 2013–2014. The geodetic transient lasted  $\sim 6$  months and produced a NW-SE trending extension of  $\sim 5.3$  mm, consistent with the regional tectonic regime. The seismicity and the geodetic signal are consistent with slip on two splay faults in the Altotiberina fault (ATF) hanging wall. Comparing the seismic moment associated with the geodetic transient and the seismic events, we observe that seismicity accounts for only a fraction of the measured geodetic deformation. The combined seismic and aseismic slip decreased the Coulomb stress on the locked shallow portion of the ATF, while the transition region to the creeping section has been loaded.

**Plain Language Summary** Among the open problems in Solid Earth Science the comprehension of earthquakes is one of the most intriguing. In order to understand how earthquakes behave it is of fundamental importance to study the whole spectrum of sizes and magnitudes. Small earthquake study is prevented because of the small deformation signals, usually covered by noise. In this work we present the study of a small seismic swarm activity in the northern Apennines (Italy), and we demonstrate that it produced observable deformation at the surface recorded by a dense geodetic network of continuous GPS. Comparing the total deformation recorded from the geodetic network and the one associated with the seismic events, we are able to determine the relative importance of seismic and aseismic motion for small earthquakes. The results indicate that aseismic deformation is not negligible, and seismic crises like the one documented must be taken into account in order to better evaluate the hazard posed by a fault.

### 1. Introduction

In order to assess the seismic potential of faults it is crucial to quantify tectonic loading rates, and the respective contribution of aseismic and seismic fault slip [e.g., Kanamori, 1977; Avouac, 2015]. In this regard, geodetic and seismic measurements are essential and seismic-aseismic interactions have been documented with such data in the last decades, mostly in high strain rate areas [e.g., Scholz et al., 1969; Marone et al., 1991; Bürgmann et al., 2001; Perfettini and Avouac, 2004, 2007; Segall et al., 2006]. One of the most evident aseismic deformation mechanisms is afterslip after a main shock [e.g., Marone et al., 1991; Donnellan and Lyzenga, 1998; Bürgmann et al., 2001; Perfettini et al., 2010]. In most of the main shock-aftershock sequences for large events ( $M_w \geq 7$ ) a significant fraction of energy (10–40% of the moment released by the main shock [e.g., Avouac, 2015, and references therein]) is released aseismically by postseismic afterslip. Smaller earthquakes can produce proportionally larger afterslip releasing a moment eventually larger than the coseismic one [e.g., Furuya and Satyabala, 2008; Langbein et al., 2006; Freed, 2007]. It has been proposed that the smaller the earthquake the greater the aseismic contribution [e.g., Fattahi et al., 2015]. This behavior is consistent with the rate-and-state friction framework: the ratio  $M_{0\text{aseismic}}/M_{0\text{seismic}}$  becomes larger if the size of the asperity (and thus the moment released seismically) decreases. Asperities of size smaller than a given threshold dimension and slowly loaded by the surrounding stable regions will always slip aseismically [Rubin and Ampuero, 2005].

Limited literature [e.g., Wicks et al., 2011; Kyriakopoulos et al., 2013; Hawthorne et al., 2016] exists on aseismic behavior associated with small seismicity ( $M_w < 5$ ), mainly because of the low signal-to-noise ratio in both

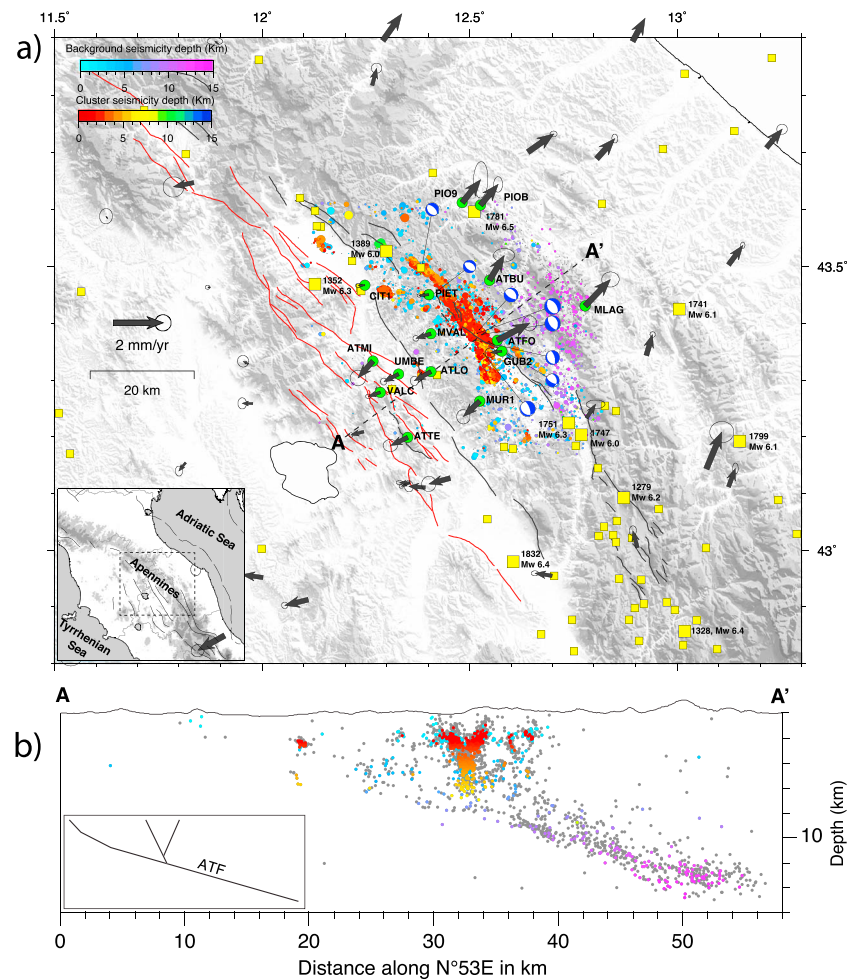


**Figure 1.** (a) Map of the study area. Arrows: residual cGPS velocities obtained after removing a pure rotation field from the Eurasian-fixed velocity field. Green circles: cGPS stations analyzed with vblCA. Red/Black lines: eastward/westward dipping fault traces (<http://ccgm.free.fr>). Gray dots: seismicity. Cold/rainbow dots: background/Clustered seismicity with  $M_w \geq M_{wC}$  (section 3.1). Focal mechanisms from <http://cnt.rm.ingv.it/tdmt>. Yellow squares: historical seismicity larger than  $M_w^{def} 5$  from *Rovida et al.* [2016]. Year and magnitude is also reported for events larger than or equal to  $M_w^{def} 6$ . Dashed line: cross section AA' (Figure 1b). Inset: regional scale map locating the area of interest (black dashed box). (b) Cross section AA'. Seismicity color code as in Figure 1a. Maximum out-of-plane distance: 5 km. Cartoon shows a schematic representation of the ATF and the two splay faults.

geodetic and seismic measurements. Since 2010, the Upper Tiber Valley hosts the Altotiberina Near Fault Observatory (NFO) (TABOO [*Chiaraluce et al.*, 2014]), a multidisciplinary research infrastructure that is now a NFO of the European Plate Observing System project. This infrastructure is composed by multisensor stations providing high-resolution geophysical (seismic, geodetic, and geochemical) data, making this region an ideal framework to study small geodetic signals occurring along normal fault segments composing a well defined system. In this work we characterize the aseismic deformation associated with a seismic swarm having a maximum recorded magnitude of  $M_w = 3.69 \pm 0.09$ , discussing the seismic and aseismic contributions that generated the observed deformation and implications of our findings.

## 2. Tectonic Setting

The ATF is an active low-angle (dip angle of  $15^\circ$ ) normal fault NNW trending and about 60 km long [e.g., *Chiaraluce et al.*, 2007] located in the Umbria-Marche sector of the northern Apennines (Figure 1a). The ATF and the faults in its hanging wall account for about 2 mm/yr out of the 3 mm/yr regional extension rate across the Apennines [*Anderlini et al.*, 2016]. Several earthquakes with default magnitude estimated from macroseismic effects  $M_w^{def} > 5.5$  are documented from historical catalogs in the Umbria-Marche region (Figure 1a),

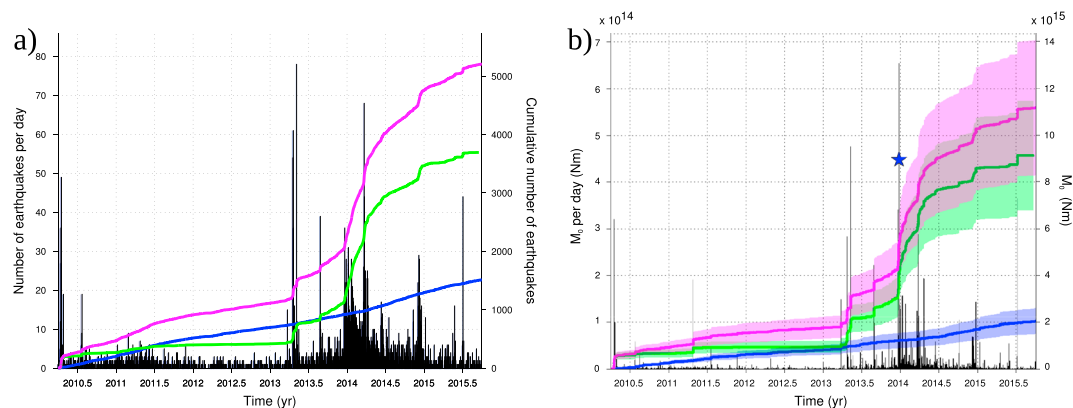


**Figure 2.** (a) Seismicity temporal evolution. Black bars: number of earthquakes per day (left y axis). Magenta/blue/green solid line: cumulative number of earthquakes belonging to the complete catalog/background seismicity/clustered seismicity (right y axis). (b) As in Figure 1 but seismic moment per day (black bars, left y axis) and cumulative seismic moment (colored lines, right y axis) are plotted instead of number of earthquakes per day and cumulative number of earthquakes, respectively. Blue star: time of the largest earthquake in the catalog (22 December 2013).

the largest event being a  $M_w^{\text{def}}$  6.4 in 1781 [Rovida *et al.*, 2016]. The ATF is aseismically creeping deeper than 5 km [Anderlini *et al.*, 2016; Vadacca *et al.*, 2016] where it is well delineated by microseismicity (Figure 1b). The larger earthquakes are thought to result from seismic slip on the shallower portion of the ATF, which is highly coupled, or along the splay faults located in its hanging wall. Local seismic monitoring revealed an increase of seismicity started in 2013 (Figure 2), rising concerns about a potential increase of strain buildup on the locked portion of the ATF.

### 3. Data

#### 3.1. Seismicity

We use the catalog of Latorre *et al.* [2016] extended to cover the April 2010 to October 2015 time span. The completeness local magnitude is  $M_{LC} = 0.6$ , and the related Gutenberg-Richter (GR)  $b$  value is  $b_L = 0.96 \pm 0.01$  (Text S1 in the supporting information). The temporal evolution of the number of earthquakes (Figure 2a) shows a seismic swarm which started with a  $M_L = 3.64 \pm 0.05$  on 18 December 2013, and lasted for about 1 year. The largest event occurred on 22 December and reached  $M_L = 3.81 \pm 0.13$  (blue star in Figure 2b). The data also include the 2010 Pietralunga sequence, documented by Marzorati *et al.* [2014] and Latorre *et al.* [2016]. The time, location, and magnitude of largest events ( $M_L > 3$ ) are listed in Table S1. In the following we focus on the 2013–2014 swarm activity.

We decluster the catalog adopting the method and parameters of Reasenber [1985]. Figure 1a shows the earthquakes spatial distribution in map view (background/clustered seismicity indicated by cold/rainbow color scale). The distribution of clustered earthquakes shows that the swarm has not activated the ATF and delineates two shallower hanging wall splay faults, one synthetic, and the other antithetic to the ATF (Figure 1b). The existence of these faults has been documented from high-resolution seismicity catalogs [e.g., Chiaraluca *et al.*, 2007; Latorre *et al.*, 2016], and the presence of a complex fault system is highlighted by seismic reflection profiles [e.g., Pialli *et al.*, 1998]. We use the hanging wall seismicity to define a planar approximation of these two faults (section 4).

Using the empirical relation of Munafó *et al.* [2016], which was determined for the study area, we convert local magnitudes into moment magnitudes and calculate the seismic moment using the relation of Hanks and Kanamori [1979]. The  $M_C$  and  $b$  value after the conversion are  $M_{wC} = 1.55$  and  $b_w = 1.440 \pm 0.015$  (Text S1). The temporal evolution of the cumulative seismic moment is shown in Figure 2b. We estimate lower and upper bounds for the seismic moment released by the swarm activity in the space and time windows where geodetic and seismic data overlap, i.e.,  $\sim 30$  km from the barycenter of clustered seismicity and from 2012.0 to 2015.7566 (Text S2). A minimum value of  $M_{0\text{ seismic}}^{\text{min}} = [0.80 \pm 0.23] \times 10^{16}$  Nm (equivalent to  $M_w^{\text{min}} = 4.53 \pm 0.08$ ) is obtained from considering only the events in the cluster with magnitude larger than  $M_{wC}$ . This estimate misses the contribution of the undetected smaller events. It also ignores the possibility that the declustering algorithm may have removed too many events. We get an upper bound of  $M_{0\text{ seismic}}^{\text{max}} = [1.44 \pm 0.29] \times 10^{16}$  Nm (equivalent

to  $M_w^{\max} = 4.70 \pm 0.06$ ) by considering the clustered seismicity for  $M_w > M_{w,c}$  and by taking into account the undetected smaller events assuming that they follow the GR distribution and that their magnitude can reach to  $-\infty$ .

### 3.2. GPS Position Time Series

The GPS data were processed adopting the three-step approach described in *Serpelloni et al.* [2006, 2013] (Text S3). The resulting position time series are analyzed taking advantage of the variational Bayesian Independent Component Analysis (vbICA) algorithm of *Choudrey and Roberts* [2003], modified and tested on GPS position time series by *Gualandi et al.* [2016a] (Text S4). We adopt the notation of *Gualandi et al.* [2016a], where the temporal evolution of the independent components (ICs) is indicated by the columns of the matrix  $V$ , the spatial distribution is associated with the corresponding columns of the matrix  $U$ , and the diagonal matrix  $S$  contains the weighting factors for each IC. The number of cGPS stations in the selected region is 15. The name and location of these stations are reported in Figure 1 and Table S2. The results of the vbICA decomposition are shown in Figure S2. We find that four ICs is the most appropriate number of component to fit the original data. The first three ICs show seasonal variations with annual and semiannual periods (Figure S3). The fourth IC shows an extensional transient signal, which is larger at MVAL and ATBU stations (Figure 3c). The displacements associated with this transient event occur parallel to the long-term extension shown by the GPS velocities in Figure 1. Here we do not attempt to interpret all the ICs, and we focus on the fourth one (IC<sub>4</sub>), which is the first nonseasonal one and which is temporally correlated with the earthquake swarm (Figure 4a). Figure 3a shows the position time series of the station MVAL as example of data on which the ICA has been performed and its ability to confidently reconstruct the observations.

## 4. Slip Model of Transient Signal

Based on the seismic catalog described in section 3.1, we define two planes within the hanging wall of the ATF (Figure 1b). We also include the ATF in order to investigate its potential role in accommodating the displacements associated with IC<sub>4</sub>. The faults are described by the parameters specified in Table S4 and are subdivided into rectangular patches.

Adopting the same approach of *Kositsky and Avouac* [2010], and replacing the principal component analysis decomposition with the ICA decomposition as in *Gualandi et al.* [2016b], we linearly invert the spatial distribution  $U_{IC_4}$  (Figure 3c) for fault slip. The Green's functions are calculated using the solutions of *Okada* [1992] for an elastic half-space, and assuming a Poisson's ratio of 0.25. The ATF plays an insignificant role in explaining the displacement signal related to IC<sub>4</sub>, which can be reconstructed by slip on the splay faults within the ATF hanging wall (Text S5 and Figure S4b). We subdivide these two faults in patches of size  $\sim 2 \times 2$  km<sup>2</sup>. The inverse problem is mixed determined, and the number of parameters to be estimated is larger than the number of data. We regularize the inverse problem following the approach of *Radiguet et al.* [2011], where an a priori null model is assumed, and let the rake to vary between 0° and  $-180^\circ$ . Such a regularization is driven by a characteristic length ( $\lambda$ ) that regulates the amount of correlation between the slip on adjacent patches, and by the uncertainty assumed on the a priori model ( $\sigma_0$ ). In the main text we show the results with  $\sigma_0 = 0.2$  m and we use a smoothing parameter  $\lambda = 1$  km that yields the best trade-off between misfit and smoothness of the slip distribution (Figure S5). Similar results are obtained with different values of  $\lambda$  and  $\sigma_0$  (Figure S6).

Recombining the result of the inversion with the weight  $S_{IC_4}$  and the temporal function  $V_{IC_4}$  we reconstruct the slip history on the fault planes associated with IC<sub>4</sub>. We obtain a maximum cumulative slip of  $15 \pm 4$  mm in the period [2012.0, 2016.0] (Figure 4c), where the uncertainty is calculated as in *Gualandi et al.* [2016b]. The fit to the horizontal displacements is excellent, with root-mean-square error (RMSE) of the order of 0.3 mm. The fit to the vertical displacements is not as good (RMSE about 0.6 mm), but still largely below the typical 5 mm uncertainty associated with the vertical GPS component.

To calculate the moment associated with the slip distribution of Figure 4c, we have to know the value of the rigidity modulus at the slip location. For the deep portion of our fault model (second and third rows of patches, i.e., between 1.7 km and 5 km) we assume a standard rigidity modulus of  $30 \pm 5$  GPa. We furthermore assume a homogeneous density and a constant Poisson ratio of 0.25, as already assumed for the calculation of the Green's functions. We derive the rigidity modulus for the shallowest line of patches (i.e., depths up to 1.7 km) using the seismic  $P$  wave velocity profile for the region, i.e., using a  $V_p$  of 4 km/s for the shallow section and  $V_p$  of 6 km/s for the deep section [*Latorre et al.*, 2016, Figure 2]. We obtain a rigidity modulus for the shallow region

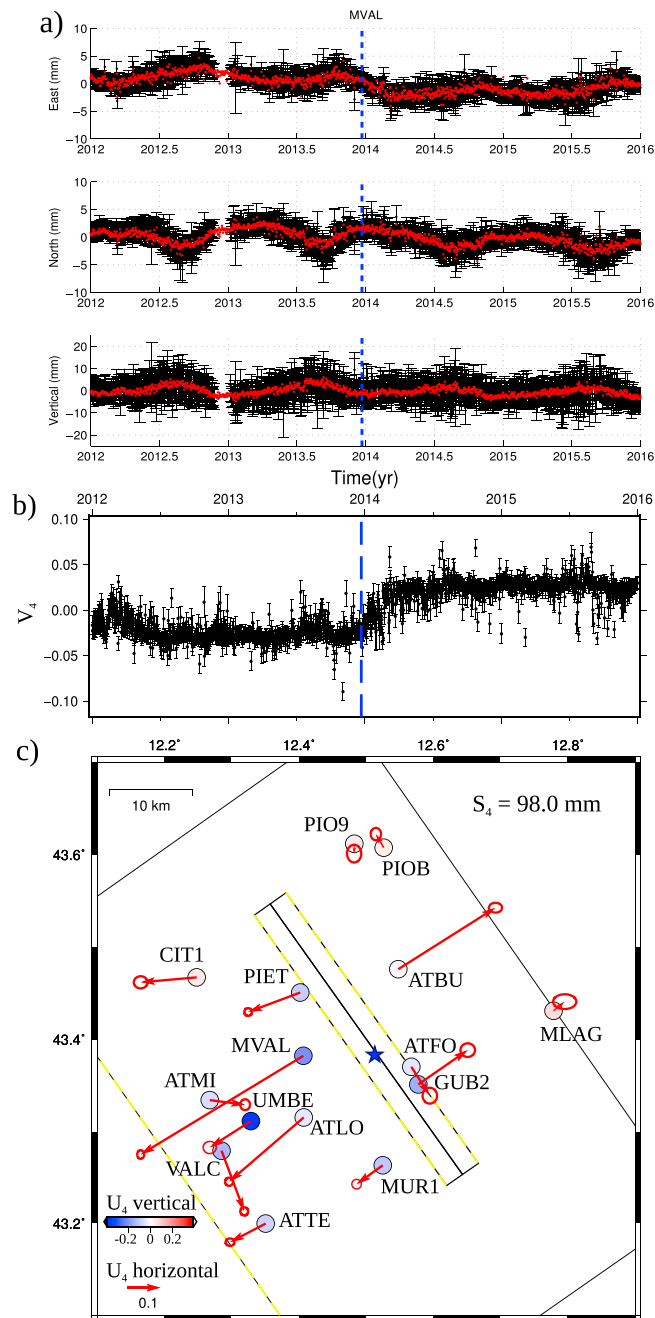


**Figure 3.** (a) Black dots and error bars: GPS position time series for the station MVAL. Red dots: ICA reconstruction. Uncertainties on the ICA reconstruction are not shown for readability. Blue dashed line indicates the epoch of the largest earthquake in the swarm. (b and c) Temporal evolution ( $V$ ) and spatial distribution ( $U$ ) of the IC related to the swarm activity and obtained performing a decomposition of the GPS position time series. The weight  $S$  is also reported (section 3.2). Black boxes: tested fault planes (ATF, synthetic, and antithetic) on which the IC has been inverted (section 4). Yellow dashed lines: Top edge of the fault planes. (b) Vertical blue line denotes time of the largest earthquake in the catalog. (c) Blue star denotes the largest event in the seismic catalog.

equal to  $13.3 \pm 2.2$  GPa. The cumulative moment associated with the slip distribution of Figure 4c is  $M_{0\text{geodetic}} = [2.44 \pm 0.22] \times 10^{16}$  Nm, equivalent to a magnitude  $M_w = 4.855 \pm 0.026$  (Figure 4b). The cumulative moment released is a robust feature of our inversion, being in the  $2\sigma$  range for all the different models:  $[2.04, 2.51] \times 10^{16}$  Nm (Figure S7). Slip in the time window where geodetic and seismic data overlap [2012.0, 2015.7566] released a moment  $M_{0\text{geodetic}} = [2.45 \pm 0.22] \times 10^{16}$  Nm. This quantity is much larger than the moment released by the swarm activity,  $M_{0\text{seismic}}$ , which we estimated to be less than  $[1.44 \pm 0.29] \times 10^{16}$  Nm (section 3.1).

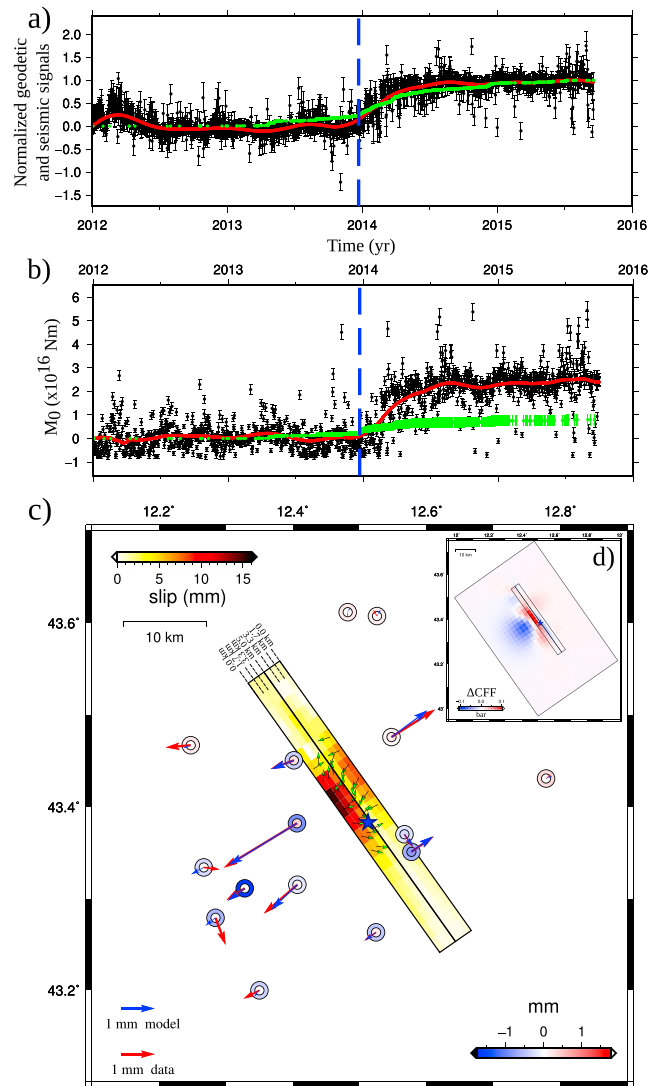


**Figure 4.** (a) Black: normalized geodetic temporal function  $V_4$  relative to  $IC_4$ . The zero is set to the median of the first year of data. Red: low-pass zero-phase filter of  $V_4$  obtained with a moving window of 90 days. Green: normalized cumulative number of clustered earthquakes. (b) Black: total (seismic + aseismic) cumulative moment released as derived from the slip model of Figure 4c. The zero is set to the median of the first year of data. Red: low-pass zero-phase filter of total cumulative moment obtained with a moving window of 90 days. Green: cumulative seismic moment for clustered events with  $M_w \geq M_{wC}$ . (c) Color palette: Cumulative slip of the best model. Fault boxes as in Figure 3. Black dashed lines: Faults' depth. Green arrows: rake direction for patches with slip >30% of maximum slip. Red vectors/outer circles: horizontal/vertical cumulative displacement associated with  $IC_4$ . Blue vectors/inner circles: horizontal/vertical cumulative displacement associated with slip model. (d) Coulomb failure function variation ( $\Delta CFF$ ) on the ATF fault due to the slip model. Receiver planes oriented for normal motion. Friction coefficient  $\mu = 0.6$ .

The moment associated with aseismic deformation ( $M_{0\text{aseismic}}$ ) can be bounded between  $[1.0 \pm 0.4] \times 10^{16}$  Nm and  $[1.6 \pm 0.3] \times 10^{16}$  Nm (Text S6). We define here the ratio  $\gamma$  as

$$\gamma = \frac{M_{0\text{aseismic}}}{M_{0\text{seismic}}} \quad (1)$$

that is estimated to be between  $[70 \pm 29]\%$  and  $[200 \pm 70]\%$ .

## 5. Discussions and Conclusions

We have detected a transient geodetic deformation signal (section 3.2) associated with a seismic swarm in a normal faulting tectonic environment. The largest cumulative horizontal displacement at the surface amounts

to only 3.3 mm (station MVAL). The detection of this small signal has been possible thanks to a dense network and the usage of the advanced vbICA multivariate statistical technique. Both the onset time and the spatial distribution of seismicity are consistent with slip occurring on secondary high-angle normal fault segments located in the hanging wall of the ATF, with the synthetic fault showing the largest slip, NNW of the largest earthquake epicenter (Figures 4c and S5). The recovered slip distribution (Figure 4c) is taking place both at shallow depths and down to the faults intersection depth, encompassing seismically active areas. The shallow aseismic slip retrieved by our inversion that is not correlated with much seismicity might be associated with aseismic deformation in Miocene turbidites which are documented in the first  $\sim 2$  km of depth [Latorre *et al.*, 2016, Figure 8 and section 3]. The clustered seismicity mainly occurred in deeper Triassic evaporites, which extend to a depth of 5 km [Latorre *et al.*, 2016, Figure 8, first row] within which some aseismic slip might also take place.

Seismic swarms such as the one observed in 2013–2014 and the associated aseismic slip should be taken into account to assess the seismic hazard posed by the ATF faults system. There is indication that such crises might return frequently enough that they can significantly contribute to the budget of moment release on these faults. Heinicke *et al.* [2006] reported a study of a seismic sequence which started in November 2001, with a maximum  $M_L$  of 4.4. Marzorati *et al.* [2014] instead detailed a sequence which started in April 2010, with a maximum  $M_L$  of 3.8. In both cases the seismically activated area was a few kilometers NW of the faults involved in 2013–2014. Such repeated crises could explain why no strong earthquake is reported in this area (Figure 1a). Since the completeness time interval for  $M_w^{\text{def}} > 6$  events in the historical seismic catalog is about 700 years for the study area [Albarelo *et al.*, 2001], the scarceness of earthquakes can be due to the fact that the accumulated stress is preferably released by swarm-like events on splay faults that are more favorably oriented for slip than the low-angle ATF. If we make the hypothesis that these kind of seismic/aseismic sequences occur regularly every 20 years and that each of them releases a moment similar to that associated with the 2013–2014 crisis, the total moment released by this tectonic activity in 1000 years is  $[1.58 \pm 0.13] \times 10^{18}$  Nm, equivalent to a  $M_w = 6.062 \pm 0.023$ . Such activity overall decreases the seismic hazard in the long term. This is not necessarily the case in the short term. As Anderlini *et al.* [2016] have already shown, the creeping sections of the ATF load the locked shallow asperities of the ATF and most of the normal splay faults in the ATF hanging wall. According to our model of fault slip during the 2013–2014 swarm, the Coulomb stress on the shallow locked portion of the ATF decreased but increased at the transition zone at about 5 km of depth (Figure 4d). This area is also the place of maximum interseismic loading [Anderlini *et al.*, 2016], and the probability to nucleate a potentially damaging earthquake there was increased by the 2013–2014 crisis despite the overall strain release.

We now discuss possible reasons for the large fraction of aseismic to seismic slip. We find a  $\gamma$  ratio between  $[70 \pm 29]\%$  and  $[200 \pm 70]\%$ , greater than what is usually found for large earthquakes ( $\gamma \sim 10\text{--}40\%$  [Avouac, 2015, and references therein]). It is, however, smaller than  $\gamma \sim 298\% \text{--} 568\%$  found for normal faulting environment by Kyriakopoulos *et al.* [2013] in Greece for a sequence of three earthquakes of magnitude 4.8, 4.6, and 4.7, respectively. In that work  $\gamma$  was probably overestimated due to the assumption of a homogeneous rigidity modulus of 30 GPa for the entire crust. If we also assume a constant rigidity modulus of 30 GPa, we would estimate  $\gamma$  between  $[120 \pm 40]\%$  and  $[290 \pm 90]\%$ , so in the range of the estimates of Kyriakopoulos *et al.* [2013]. Our results are consistent with those of Hawthorne *et al.* [2016], even if obtained with completely different techniques and observations in a different tectonic context.

Given the small amplitude of the geodetic signal and the small size and frequency of the earthquakes, we cannot extract the signal associated with individual earthquakes. We cannot therefore test if the large aseismic slip in our study area is due to disproportionately large afterslip or preseismic slip associated with the small earthquakes, or a transient aseismic event which would be driving small subsidiary earthquakes. Assessing if a fraction of aseismic slip is preceding the seismic rupture would shed important light on the mechanisms that play a role in earthquake nucleation and triggering. Preseismic slip is observed in laboratory experiments and therefore predicted by earthquake nucleation models which were derived from such experimental data, in particular those based on rate-and-state friction [Dieterich, 1994]. Such models imply an aseismic nucleation phase until the slipping area reaches a large enough size for a runaway seismic rupture. If the size of a rate-weakening patch decreases to the nucleation size, the ratio of aseismic to seismic slip on that patch becomes infinite. This behavior is observed, for example, in the numerical simulations of Chen and Lapusta [2009], which were designed to reproduce repeating earthquakes in the range  $0.25 \leq M_w \leq 3.67$ . The parameters chosen in that simulation imply a critical magnitude of about  $M_w^* \sim 1.26$  ( $M_0^* \sim 10^{11}$  Nm). The seismicity presented in our work ranges from  $M_{w,C} = 1.55$  to  $3.69 \pm 0.09$ , i.e., above the critical magnitude  $M_w^*$  tested

by Chen and Lapusta [2009]. The empirical  $\gamma$  ratio documented in our work is representative of the entire sequence, and not of a single earthquake, but it agrees with the ratio between the moment released aseismically and seismically over a rate-weakening patch between 25% and 400% observed in the numerical simulations. Moreover, we estimated the  $\gamma$  ratio considering the slip on the entire fault, and not only on the rate-weakening asperity as in Chen and Lapusta [2009]. This means that their calculations can be seen as a lower bound for  $\gamma$ . Further investigation of the role of aseismic slip preceding seismic ruptures on the ATF fault system would require additional instrumentation such as, for example, borehole strainmeters, which would allow to measure smaller strain at a higher sampling rate than what is possible with GPS. Moreover, a reduction in the completeness magnitude ( $M_{w,c} < M^*$ ) would be required in order to test the prediction from the rate-and-state friction at small scales, for which aseismic deformation becomes dominant at small enough patch sizes.

The presence of pressurized fluids could provide another possible explanation for the prolonged swarm-like seismic activity and large aseismic contribution that we observe in this study. There are experimental and observational evidences from various tectonic contexts that high pore pressure tends to promote aseismic creep [Bourouis and Bernard, 2007; Lohman and McGuire, 2007; Cappa et al., 2009; Wicks et al., 2011; Moreno et al., 2014; Guglielmi et al., 2015; Wei et al., 2015]. These evidences are consistent with the fact that at high pore pressure, it is also expected to promote aseismic creep in the rate-and-state framework [e.g., Avouac, 2015]. For example, Wicks et al. [2011] studied a seismic swarm in the Columbia River flood basalts (United States) with an equivalent magnitude  $M_w = 4.0$ . From interferometric synthetic aperture radar data they found a geodetic moment eight times the seismic one, indicating that the swarm might have been driven by fluid pore pressure variations. In the context of the ATF, fluids might well play a role. In this sector of the Apennines there is indeed evidence for degassing of  $\text{CO}_2$  [Chiodini et al., 2000]. Chiodini and Cioni [1989] reported  $\text{CO}_2$  pressures in 3.7 km and 4.7 km depth boreholes at 85% of the lithostatic load, and some studies suggested an association with seismicity [Miller et al., 2004; Chiodini et al., 2004; Collettini et al., 2008]. It is thus possible that the origin and driving mechanisms explaining the swarm documented in this study may be better unraveled by taking into account the presence of migrating fluids.

#### Acknowledgments

Some Figures have been created with the Generic Mapping Tool [Wessel et al., 2013]. The declustering has been performed using the Matlab software ZMAP [Wiemer, 2001]. We thank Raffaele Di Stefano for his valuable contribution in the seismic catalog generation. A.G. received financial support through the National Science Foundation (NSF) Geophysical Proposal ID 145136. This work has been developed also in the framework of the project TRANSIENTI, founded by the Italian Ministry of Education, Universities and Research (MIUR)-Premiale 2014. We are grateful to all public and private institutions that made the continuous GPS data used in this work available (<http://ring.gm.ingv.it>; <http://www.umbriageo.regione.umbria.it>; <http://www.netgeo.it>; <http://smartnet.leica-geosystems.it>). GPS time series are available as supporting information. We thank TABOO Near Fault Observatory site managers for data care and availability. The seismic catalog can be obtained by contacting L.C. ([lauro.chiaraluca@ingv.it](mailto:lauro.chiaraluca@ingv.it)).

#### References

- Albarelo, D., R. Camassi, and A. Rebez (2001), Detection of space and time heterogeneity in the completeness of a seismic catalog by a statistical approach: An application to the Italian area, *Bull. Seismol. Soc. Am.*, *91*(6), 1694–1703, doi:10.1785/0120000058.
- Anderlini, L., E. Serpelloni, and M. Belardinelli (2016), Creep and locking of a low-angle normal fault: Insights from the Altotiberina fault in the Northern Apennines (Italy), *Geophys. Res. Lett.*, *43*, 221–4329, doi:10.1002/2016GL068604.
- Avouac, J.-P. (2015), From geodetic imaging of seismic and aseismic fault slip to dynamic modeling of the seismic cycle, *Annu. Rev. Earth Planet. Sci.*, *43*, 233–71, doi:10.1146/annurev-earth-060614-105302.
- Bourouis, S., and P. Bernard (2007), Evidence for coupled seismic and aseismic fault slip during water injection in the geothermal site of Soultz (France), and implications for seismogenic transients, *Geophys. J. Int.*, *169*(2), 723–732.
- Bürgmann, R., M. Kogan, V. Levin, C. Scholz, R. King, and G. Steblov (2001), Rapid aseismic moment release following the 5 December, 1997 Kronotsky, Kamchatka, earthquake, *Geophys. Res. Lett.*, *28*(7), 1331–1334.
- Cappa, F., J. Rutqvist, and K. Yamamoto (2009), Modeling crustal deformation and rupture processes related to upwelling of deep  $\text{CO}_2$ -rich fluids during the 1965–1967 Matsushiro earthquake swarm in Japan, *J. Geophys. Res.*, *114*, B10304, doi:10.1029/2009JB006398.
- Chen, T., and N. Lapusta (2009), Scaling of small repeating earthquakes explained by interaction of seismic and aseismic slip in a rate and state fault model, *J. Geophys. Res.*, *114*, B01311, doi:10.1029/2008JB005749.
- Chiaraluca, L., C. Chiarabba, C. Collettini, D. Piccinini, and M. Cocco (2007), Architecture and mechanics of an active low-angle normal fault: Alto Tiberina Fault, northern Apennines, Italy, *J. Geophys. Res.*, *112*, B10310, doi:10.1029/2007JB005015.
- Chiaraluca, L., et al. (2014), The Alto Tiberina Near Fault Observatory (northern Apennines, Italy), *Ann. Geophys.*, *57*(3), S0327, doi:10.4401/ag-6426.
- Chiodini, G., and R. Cioni (1989), Gasgeobarometry for hydrothermal systems and its application to various Italian geothermal areas, *Appl. Geochem.*, *4*, 465–472.
- Chiodini, G., F. Frondini, C. Cardellini, F. Parello, and L. Peruzzi (2000), Rate of diffuse carbon dioxide Earth degassing estimated from carbon balance of regional aquifers: The case of central Apennines, Italy, *J. Geophys. Res.*, *105*(B4), 8423–8434.
- Chiodini, G., C. Cardellini, A. Amato, E. Boschi, S. Caliro, F. Frondini, and G. Ventura (2004), Carbon dioxide Earth degassing and seismogenesis in central and southern Italy, *Geophys. Res. Lett.*, *31*, L07615, doi:10.1029/2004GL019480.
- Choudrey, R., and S. Roberts (2003), Variational mixture of bayesian independent component analyzers, *Neural Comput.*, *15*(1), 213–252.
- Collettini, C., C. Cardellini, G. Chiodini, N. D. Paola, R. Holdsworth, and S. Smith (2008), Fault weakening due to  $\text{CO}_2$  degassing in the Northern Apennines: short- and long-term processes, *Geol. Soc.*, *299*, 175–194, doi:10.1144/SP299.11.
- Dieterich, J. (1994), A constitutive law for the rate of earthquake production and its application to earthquake clustering, *J. Geophys. Res.*, *99*, 2601–2618.
- Donnellan, A., and G. Lyzenga (1998), GPS observations of fault afterslip and upper crustal deformation following the Northridge earthquake, *J. Geophys. Res.*, *103*(B9), 21,285–21,297.
- Fattahi, H., F. Amelung, E. Chaussard, and S. Wdowinski (2015), Coseismic and postseismic deformation due to the 2007  $M_{5.5}$  Ghazaband fault earthquake, Balochistan, Pakistan, *Geophys. Res. Lett.*, *42*, 3305–3312, doi:10.1002/2015GL063686.
- Freed, A. (2007), Afterslip (and only afterslip) following the 2004 Parkfield, California, earthquake, *Geophys. Res. Lett.*, *34*, L06312, doi:10.1029/2006GL029155.

- Furuya, M., and S. Satyabala (2008), Slow earthquake in Afghanistan detected by InSAR, *Geophys. Res. Lett.*, *35*, L06309, doi:10.1029/2007GL033049.
- Gualandi, A., E. Serpelloni, and M. Belardinelli (2016a), Blind source separation problem in GPS time series, *J. Geodesy*, *90*(4), 323–341, doi:10.1007/s00190-015-0875-4.
- Gualandi, A., et al. (2016b), Pre- and post-seismic deformation related to the 2015,  $M_w$  7.8 Gorkha Earthquake, Nepal, *Tectonophysics*, doi:10.1016/j.tecto.2016.06.014.
- Guglielmi, Y., F. Cappa, J.-P. Avouac, P. Henry, and D. Elsworth (2015), Seismicity triggered by fluid injection-induced aseismic slip, *Science*, *348*(6240), 1224–1226, doi:10.1126/science.aab0476.
- Hanks, T., and H. Kanamori (1979), A moment magnitude scale, *J. Geophys. Res.*, *84*(B5), 2348–2350.
- Hawthorne, J., M. Simons, and J. Ampuero (2016), Estimates of aseismic slip associated with small earthquakes near San Juan Bautista, CA, *J. Geophys. Res. Solid Earth*, *121*, 8254–8275, doi:10.1002/2016JB013120.
- Heinicke, J., T. Braun, P. Burgassi, F. Italiano, and G. Martinelli (2006), Gas flow anomalies in seismogenic zones in the Upper Tiber Valley, Central Italy, *Geophys. J. Int.*, *167*, 794–806.
- Kanamori, H. (1977), Seismic and Aseismic slip along subduction zones and their tectonic implications, in *Island Arcs, Deep Sea Trenches and Back-Arc Basins*, edited by M. Talwani and W. C. Pitman, pp. 163–174, AGU, Washington, D. C., doi:10.1029/ME001p0163.
- Kositsky, A., and J.-P. Avouac (2010), Inverting geodetic time series with a principal component analysis-based inversion method, *J. Geophys. Res.*, *115*, B03401, doi:10.1029/2009JB006535.
- Kyriakopoulos, C., M. Chini, C. Bignami, S. Stramondo, A. Ganas, M. Kolligri, and A. Moshou (2013), Monthly migration of a tectonic seismic swarm detected by DInSAR: southwest Peloponnese, Greece, *Geophys. J. Int.*, *194*, 1302–1309, doi:10.1093/gji/ggt196.
- Langbein, J., J. Murray, and H. Snyder (2006), Coseismic and initial postseismic deformation from the 2004 Parkfield, California, earthquake, observed by Global Positioning System, creepmeters, and borehole strainmeters, *Bull. Seism. Soc. Am.*, *96*(4B), S304–S320.
- Latorre, D., F. Mirabella, L. Chiaraluca, F. Trippetta, and A. Lomax (2016), Assessment of earthquake locations in 3-D deterministic velocity models: A case study from the Altotiberina Near Fault Observatory (Italy), *J. Geophys. Res. Solid Earth*, *121*, 8113–8135, doi:10.1002/2016JB013170.
- Lohman, R., and J. McGuire (2007), Earthquake swarms driven by aseismic creep in the Salton Trough, California, *J. Geophys. Res.*, *112*, B04405, doi:10.1029/2006JB004596.
- Marone, C., C. Scholz, and R. Bilham (1991), On the mechanics of earthquake afterslip, *J. Geophys. Res.*, *96*(B5), 8441–8452.
- Marzorati, S., M. Massa, M. Cattaneo, G. Monachesi, and M. Frapiccini (2014), Very detailed seismic pattern and migration inferred from the April 2010 Pietralunga (northern Italian Apennines) micro-earthquake sequence, *Tectonophysics*, *610*, 91–109, doi:10.1016/j.tecto.2013.10.014.
- Miller, S., C. Collettini, L. Chiaraluca, M. Cocco, M. Barchi, and B. Kaus (2004), Aftershocks driven by a high-pressure  $CO_2$  source at depth, *Nature*, *427*(6976), 724–727, doi:10.1038/nature02251.
- Moreno, M., C. Haberland, O. Oncken, A. Rietbrock, S. Angiboust, and O. Heidbach (2014), Locking of the Chile subduction zone controlled by fluid pressure before the 2010 earthquake, *Nat. Geosci.*, *7*(4), 292–296, doi:10.1029/2007JB005424.
- Munafó, I., L. Malagnini, and L. Chiaraluca (2016), On the relationship between  $M_w$  and  $M_L$  for small earthquakes, *Bull. Seismol. Soc. Am.*, *106*(5), 2402–2408, doi:10.1785/0120160130.
- Okada, Y. (1992), Internal deformation due to shear and tensile faults in a half-space, *Bull. Seismol. Soc. Am.*, *82*(2), 1018–1040.
- Perfettini, H., and J.-P. Avouac (2004), Postseismic relaxation driven by brittle creep: A possible mechanism to reconcile geodetic measurements and the decay rate of aftershocks, application to the Chi-Chi earthquake, *J. Geophys. Res.*, *109*, B02304, doi:10.1029/2003JB002488.
- Perfettini, H., and J.-P. Avouac (2007), Modeling afterslip and aftershocks following the 1992 Landers earthquake, *J. Geophys. Res.*, *112*, B07409, doi:10.1029/2006JB004399.
- Perfettini, H., et al. (2010), Seismic and aseismic slip on the Central Peru megathrust, *Nature*, *465*(7294), 78–81, doi:10.1038/nature09062.
- Piaili, G., M. Barchi, and G. Minelli (1998), Results of the CROP03 deep seismic reflection profile, *Mem. Soc. Geol. Ital.*, *52*, 1–657.
- Radiguet, M., F. Cotton, M. Vergnolle, M. Campillo, B. Valette, V. Kostoglodov, and N. Cotte (2011), Spatial and temporal evolution of a long term slow slip event: The 2006 Guerrero Slow Slip Event, *Geophys. J. Int.*, *184*, 816–828, doi:10.1111/j.1365-246X.2010.04866.x.
- Reasenber, P. (1985), Second-order moment of central California seismicity, 1969–82, *J. Geophys. Res.*, *90*, 5479–5495.
- Rovida, A., M. Locati, R. Camassi, B. Lolli, and P. Gasperini (2016), *CPT15, the 2015 Version of the Parametric Catalogue of Italian Earthquakes*, Istituto Nazionale di Geofisica e Vulcanologia, doi:10.6092/INGV.IT.
- Rubin, A., and J.-P. Ampuero (2005), Earthquake nucleation on (aging) rate and state faults, *J. Geophys. Res.*, *110*, B11312, doi:10.1029/2005JB003686.
- Scholz, C., M. Wyss, and S. Smith (1969), Seismic and aseismic slip on the San Andreas fault, *J. Geophys. Res.*, *74*(8), 2049–2069.
- Segall, P., E. Desmarais, D. Shelly, A. Miklius, and P. Cervelli (2006), Earthquakes triggered by silent slip events on Kilauea volcano, Hawaii, *Nature*, *442*(7098), 71–74.
- Serpelloni, E., G. Casula, A. Galvani, M. Anzidei, and P. Baldi (2006), Data analysis of permanent GPS networks in Italy and surrounding regions: application of a distributed processing approach, *Ann. Geophys.*, *49*(45), 897–928.
- Serpelloni, E., C. Faccenna, G. Spada, D. Dong, and S. Williams (2013), Vertical GPS ground motion rates in the Euro-Mediterranean region: New evidence of velocity gradients at different spatial scales along the Nubia-Eurasia plate boundary, *J. Geophys. Res. Solid Earth*, *118*, 6003–6024, doi:10.1002/2013JB010102.
- Vadacca, L., E. Casarotti, L. Chiaraluca, and M. Cocco (2016), On the mechanical behaviour of a low-angle normal fault: The Alto Tiberina fault (Northern Apennines, Italy) system case study, *Solid Earth*, *7*, 1537–1549, doi:10.5194/se-7-1537-2016.
- Wei, S., et al. (2015), The 2012 Brawley swarm triggered by injection-induced aseismic slip, *Earth Planet. Sci. Lett.*, *422*, 115–125.
- Wessel, P., W. Smith, R. Scharroo, J. Luis, and F. Wobbe (2013), Generic mapping tools: Improved version released, *EOS, Trans, AGU*, *94*, 409–410.
- Wicks, C., W. Thelen, C. Weaver, J. Gombert, A. Rohay, and P. Bodin (2011), InSAR observations of aseismic slip associated with an earthquake swarm in the Columbia River flood basalts, *J. Geophys. Res.*, *116*, B12304, doi:10.1029/2011JB008433.
- Wiemer, S. (2001), A software package to analyze seismicity: ZMAP, *Seismol. Res. Lett.*, *72*(3), 373–382, doi:10.1785/gssrl.72.3.373.